with the crystal mosaicity and anisotropy of the data. The current structure consists of residues 2–121 and 82 waters with 92% of the residues in favoured regions of the Ramachandran plot, 6% in generously allowed regions and 2% in unfavoured regions[27]. Residues Ile 104 and Ala 118 are the two outliers; Ile 104 lies in the tight turn between α4B and the C-loop; and Ala 118 has weak density along with residues 116–121

Crystallization of the SarA–DNA complex

We used a number of deoxyoligonucleotides in crystallization trials with SarA, and only those with an 8-mer duplex yielded data-quality crystals. We grew these crystals using hanging drop/vapour diffusion with a crystallization solution of 25% PEG 8000, 200 mM $CaCl_2$, 100 mM cacodylate, pH 6.5. They are monoclinic, space group $P2_1$, with $a = 54.5$ Å, $b = 65.2$ Å, $c = 57.8$ Å and $\beta = 118.0°$ and contain one SarA dimer and 8-mer duplex per asymmetric unit. All data were collected at room temperature with an ADSC multiwire area detector[28] and a RIGAKU RU200-H rotating anode X-ray generator with graphite monochromator operating at 40 kV and 150 mA.

Structure determination and refinement

Because of DNA disorder, iodinated deoxyoligonucleotides failed as derivatives, therefore phases were derived from a thimerosal derivative in conjunction with twofold averaging and solvent flattening[24]. Density was evident for the α1 and α4A helices and the backbone of helices α2 and α3. However, in averaged maps, the density for α4B was smeared and subsequently phase-combined; unaveraged maps revealed different orientations of these helices. The density for the phosphate backbone of 6 bp in the centre of the DNA-binding channel was also evident (Fig. 5). Good electron density was also observed for the bases but their identities were ambiguous and therefore, fitted with alternating A·T base pairs ($5'$-$A_1T_2A_3T_4A_5T_6A_7$-$3'$). We then subjected the structure to positional and tightly restrained *B*-factor refinement[26]. The current model includes residues 2–113 of one subunit and 2–121 of the other, and a 6-bp duplex with 3′-adenylate nucleotide overhangs. Analysis of the Ramachandran plot shows that 94% of the residues are in the most favoured regions, 5.5% in generously allowed regions and 0.5% in unfavoured regions (Phe 30 from one subunit is the outlier)[27]. Two large solvent peaks were located in the DNA minor-groove binding site. Their thermal parameters indicated that they are Ca^{2+} ions, which is consistent with the observation that either magnesium or calcium is required for crystallization of the SarA–DNA complex. Residual density in the DNA-binding channel indicates additional disordered DNA in the binding site. Although the gripper helices α4B and α4B′ take different orientations, residues 5–95 of each subunit overlay with r.m.s. deviations of 0.55 Å.

Received 10 August; accepted 16 October 2000.

1. Projan, S. L. & Novickn, R. P. in *Staphylococci in Human Disease* (eds Cross, K. B. & Archer, G. L.) 55–81 (Churchill Livingstone, New York, 1997).
2. Cheung, A. L., Koomey, J. M., Butler, C. A., Projan, S. J. & Fischetti, V. A. Regulation of exoprotein expression in *Staphylococcus aureus* by a locus (*sar*) distinct from *agr*. *Proc. Natl Acad. Sci. USA* **89,** 6462–6466 (1992).
3. Cheung, A. L. & Projan, S. J. Cloning and sequencing of *sarA* of *Staphylococcus aureus*, a gene required for expression of *agr*. *J. Bacteriol.* **176,** 4168–4172 (1994).
4. Morfeldt, E., Tegmark, K. & Arvidson, S. Transcriptional control of the *agr*-dependent virulence gene regulator, RNAIII, in *Staphylococcus aureus*. *Mol. Microbiol.* **21,** 1227–1237 (1996).
5. Wolz, C. *et al*. *Agr*-independent regulation of fibronectin-binding protein(s) by the regulatory locus *sar* in *Staphylococcus aureus*. *Mol. Microbiol.* **36,** 230–243 (2000).
6. Cheung, A. & Ying, P. Regulation of α- and β-hemolysins by the *sar* locus of *Staphylococcus aureus*. *J. Bacteriol.* **176,** 580–585 (1994).
7. Blevins, J. S., Gillaspy, A. F., Rechtin, T. M., Hurlbert, B. K. & Smeltzer, M. S. The staphylococcal accessory gene regulator (*sar*) represses transcription of the *Staphylococcus aureus* collagen adhesin gene (*cna*) in an *agr*-independent manner. *Mol. Microbiol.* **33,** 317–326 (1999).
8. Gaskill, M. E. & Khan, S. A. Regulation of the enterotoxin B gene in *Staphylococcus aureus*. *J. Biol. Chem.* **263,** 6276–6280 (1988).
9. Manna, A. C., Bayer, M. G. & Cheung, A. L. Transcriptional analysis of different promoters in the *sar* locus in *Staphylococcus aureus*. *J. Bacteriol.* **180,** 3828–3836 (1998).
10. Chien, Y.-t., Manna, A., Projan, S. J. & Cheung, A. L. SarA, a global regulator of virulence determinants in *Staphylococcus aureus*, binds to a conserved motif essential for *sar*-dependent gene regulation. *J. Biol. Chem.* **274,** 37169–37176 (1999).
11. Rechtin, T. M. *et al*. Characterization of the SarA virulence gene regulator of *Staphylococcus aureus*. *Mol. Microbiol.* **33,** 307–316 (1999).
12. Holm, L. & Sander, C. Protein structure comparisons by alignment of distance matrices. *J. Mol. Biol.* **233,** 123–138 (1993).
13. Heinrichs, J. H., Bayer, M. G. & Cheung, A. L. Characterization of the *sar* locus and its interactions with *agr* in *Staphylococcus aureus*. *J. Bacteriol.* **178,** 418–423 (1996).
14. Lavery, R. & Sklenar, H. J. The definition of generalized helicoidal parameters and of axis curvature for irregular nucleic acids. *Biomol. Struct. Dynam.* **6,** 63–91 (1988).
15. Saenger, W. *Principles of Nucleic Acid Structure* (Springer, New York, 1984).
16. Mahendrasingam, A. *et al*. Time-resolved X-ray diffraction studies of the B ↔ D structural transition in the DNA double helix. *Science* **233,** 195–197 (1986).
17. Baxevanis, A. D. & Vinson, C. R. Interactions of coiled coils in transcription factors: where is the specificity? *Curr. Opin. Genet. Dev.* **3,** 278–285 (1993).
18. Pruss, G. & Drlica, K. DNA supercoiling and prokaryotic transcription. *Cell* **56,** 521–523 (1989).
19. Record, M. T. Jr, Reznikoff, W. S., Craig, M. L., McQuade, K. L. & Schlax, P. J. in *Escherichia coli and Salmonella: Cellular and Molecular Biology* (eds Neidhardt, F. C. *et al.*) 792–820 (ASM, Washington DC, 1996).
20. Oberto, J., Drlica, K. & Rouviere-Yaniv, J. Histones, HMG, HU, IHF: Meme combat. *Biochemie* **76,** 901–908 (1994).
21. Chan, P. F. & Foster, S. J. Role of SarA in virulence determinant production and environmental signal transduction in *Staphylococcus aureus*. *J. Bacteriol.* **180,** 6232–6241 (1998).
22. Hendrickson, W. A. Determination of macromolecular structures from anomalous diffraction of synchrotron radiation. *Science* **254,** 51–58 (1991).
23. Collaborative computational project number 4. *J. Appl. Crystallogr. D* **50,** 760 (1994).
24. Furey, W. B. & Swaminathan, S. PHASE-95: a program package for the processing and analysis of diffraction data from macromolecules. In ;*Methods in Enzymol*. **Vol. 277** (eds Carter, C. W. & Sweet, R. M.) 590–620 (Academic, Orlando, 1997).
25. Jones, T. A., Zou, J.-Y., Cowan, S. W. & Kjeldgaard, M. Improved methods for building protein models in electron density maps and the location of errors in these models. *Acta. Crystallogr. A* **47,** 110–119 (1991).
26. Tronrud, D. E., TenEyck, L. F. & Matthews, B. W. An efficient general purpose least-squares refinement program for macromolecular structures. *Acta. Crystallogr. A* **43,** 489–501 (1985).
27. Laskowski, R. A., MacArthur, M. W. & Thorton, J. M. PROCHECK: a program to check the stereochemical quality of protein structures. *J. Appl. Cryst.* **26,** 283–291 (1993).
28. Howard, A. J., Nielson, C. & Xuong, N. H. Software for a diffractometer with multiwire area detector. *Methods Enzymol.* **114,** 452–472 (1985).
29. Nicholls, A., Sharp, K. & Honig, B. H. Protein folding and association: insights from the interfacial and thermodynamic properties of hydrocarbons. *Proteins* **11,** 281–296 (1991).

Acknowledgements

We thank M. S. Smeltzer for his critical reading of this manuscript. Intensity data collected at the Stanford Synchrotron Radiation Laboratory (SSRL) was carried out under the SSRL biotechnology program, which is supported by the National Institutes of Health (NIH), National Center for Research Resources, Biomedical Technology Program, and by the Department of Energy, Office of Biological and Environmental Research. M.A.S. is a Burroughs Wellcome Career Awardee. This work was supported by the NIH Oregon Health Sciences Foundation (R.G.B.).

Correspondence and requests for materials should be addressed to R.G.B (e-mail: brennanr@ohsu.edu). The refined coordinates for the SarA structure and SarA–DNA complex have been deposited with the Protein Data Bank under accession codes 1FZN and 1FZP, respectively.

Projection structure of a ClC-type chloride channel at 6.5 Å resolution

Joseph A. Mindell*, Merritt Maduke*, Christopher Miller* & Nikolaus Grigorieff*†

** Department of Biochemistry, Howard Hughes Medical Institute and † Rosenstiel Basic Medical Science Research Center and W. M. Keck Institute for Cellular Visualization, Brandeis University, Waltham, Massachusetts 02454, USA*

Virtually all cells in all eukaryotic organisms express ion channels of the ClC type, the only known molecular family of chloride-ion-selective channels. The diversity of ClC channels highlights the multitude and range of functions served by gated chloride-ion conduction in biological membranes, such as controlling electrical excitability in skeletal muscle, maintaining systemic blood pressure, acidifying endosomal compartments, and regulating electrical responses of GABA (γ-aminobutyric acid)-containing interneurons in the central nervous system[1]. Previously, we expressed and purified a prokaryotic ClC channel homologue[2]. Here we report the formation of two-dimensional crystals of this ClC channel protein reconstituted into phospholipid bilayer membranes. Cryo-electron microscopic analysis of these crystals yields a projection structure at 6.5 Å resolution, which shows off-axis water-filled pores within the dimeric channel complex.

Of the approximately ten ClC isoforms found in eukaryotes, the muscle subtypes ClC-0 and ClC-1 are by far the most thoroughly studied. These voltage-gated channels are homodimers of polypeptides with a relative molecular mass of 90,000 that contain 10–12 putative transmembrane segments[3]. Detailed single-channel analysis indicates that these channels are double-barrelled homodimers in which the functional dimer contains two identical pores devoid of axial symmetry, each with its own voltage-dependent gate[4–8]. It is not known, however, whether this unusual molecular architecture applies to all ClC channels or only to the muscle subfamily. Moreover, this picture is not universally accepted; recently, a conventional

barrel-stave architecture for ClC-1 was proposed, with a single pore formed on the homodimer's two-fold axis[9]. Such fundamentally discordant views are best resolved with direct structural information; the recent overexpression, purification and functional reconstitution of EriC, a prokaryotic ClC channel[2], provides opportunities for structural approaches to the problem.

We produced two-dimensional crystals of EriC by reconstituting the purified channel protein into phospholipid membranes at high protein-to-lipid ratio. The crystals, which form spontaneously during removal of detergent by dialysis over several days, appear in large sheets up to 4 μm on a side (Fig. 1a) containing 10^4–10^5 EriC channels; most of the material in these samples is crystalline, as gauged by optical diffraction of negatively stained electron microscope images. Although double and multi-layer crystals are often observed, single-layered sheets are common, and only these were analysed here.

Before beginning structural analysis, we assessed whether the crystallization process irreversibly damages the protein. Crystalline EriC was solublized in detergent and reconstituted back into lipid vesicles at much lower protein density, so that each vesicle carries approximately a single EriC channel. Efflux of $^{36}Cl^-$ from these vesicles was then assayed by a method designed to quantify the fraction of protein in the preparation that is functionally active[2]. Figure 1b shows that EriC recovered from crystals is indistinguishable in activity from EriC that had never been crystallized. This result gives us confidence as to the integrity of the protein in the crystals.

The computed diffraction pattern of unstained, glucose-embedded EriC crystals (Fig. 2a) reveals an orthorhombic unit cell with dimensions of 140 × 80 Å. Systematic absences of odd axial reflections suggest glide planes along both axes. These low-dose images show strong reflections to ~8.5 Å by optical diffraction, and after correction for lattice distortions yield significant data to at least 5 Å; in addition, electron diffraction produces reflections to 4 Å (data not shown). For all images, analysis of the phases of symmetry-related spots[10] of both raw and processed transforms places the crystals in the two-sided plane group $P22_12_1$. Inspection of computationally filtered but unsymmetrized images (Fig. 2b) further confirms $P22_12_1$ symmetry, which arises from packing of near neighbours in opposite transmembrane orientations.

From about 80 micrographs, 7 were chosen for further processing. The crystalline areas of these images were corrected for lattice distortions, merged and averaged in $P22_12_1$. Crystallographic parameters are reported in Table 1, and Fig. 3 indicates the quality

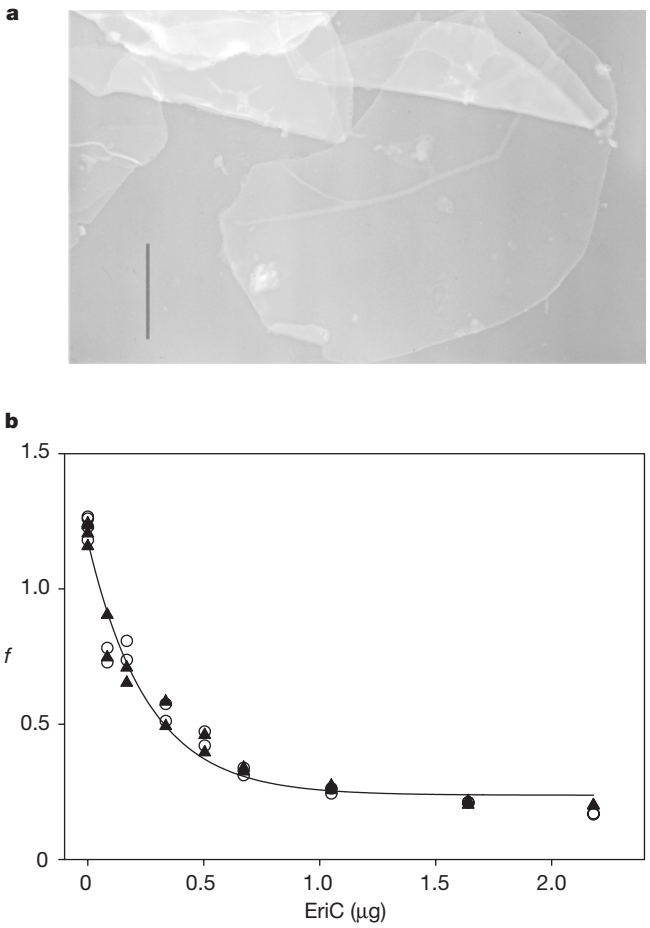

Figure 1 Active 2D crystals of EriC. **a**, Electron microscopic image of crystals embedded in 1% uranyl acetate stain. Scale bar, 1 μm. **b**, Functional activity of EriC after crystallization. The fractional trapped $^{36}Cl^-/^3H$[glutamate] ratio, *f*, was determined for vesicles reconstituted with the indicated amount of EriC (closed triangles) or EriC extracted from the 2D crystals (open circles). The solid curve represents the variation expected from a Poisson distribution of protein in vesicles[2].

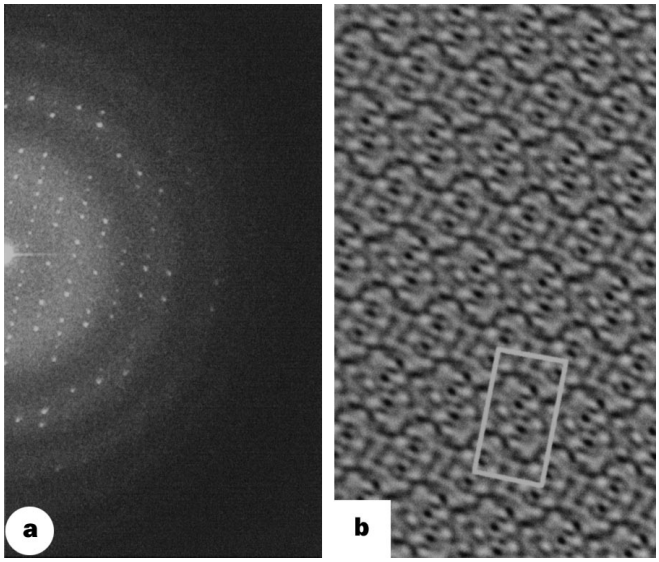

Figure 2 Analysis of glucose-embedded EriC crystals. **a**, Computed diffraction pattern from a single cryo-electron microscope image of an EriC crystal, showing strong spots out to ~8.5 Å resolution. **b**, Digitally filtered image of EriC crystal. The diffraction pattern in **a** was filtered by removing all data not on the reciprocal lattice. This masked transform was then corrected for the CTF and reverse Fourier transformed to yield an image of the crystal. In this grey-scale image, higher scattering densities are brighter, and lower densities are darker. A single unit cell is boxed.

Table 1 Electron crystallographic image statistics

Two-sided plane group symmetry	$P22_12_1$
Unit cell dimensions	*a* = 140 Å
	b = 80 Å
	γ = 90°
Number of images and lattices	7
Range of defocus	4,280–8,390 Å
Total number of reflections	1,766
Number of unique reflections	204
Overall phase residual to 6.5 Å (random = 45°)	12.5°

Resolution range (Å)	Number of unique reflections	Phase residual (random = 45°)
100–10.01	84	4.2
10.0–8.01	51	9.9
8.0–7.01	42	22.1
7.0–6.51	27	28.4
6.5–6.01	36	36.1
6.0–5.0	94	40.8

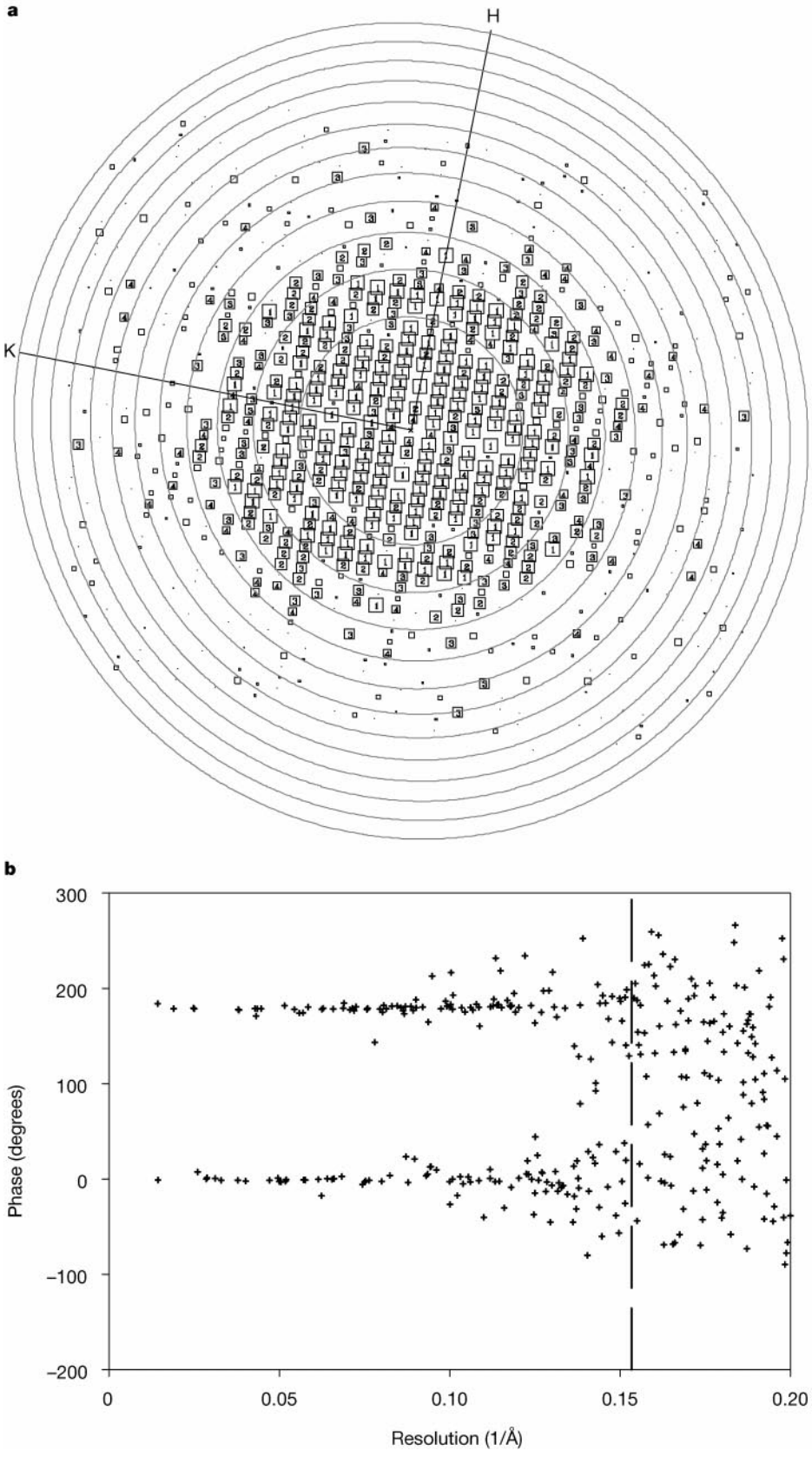

Figure 3 Quality of diffraction data. **a**, Plot of diffraction spots from the image described in Fig. 2, after correction for crystal distortion. Each spot in the transform is represented by a square and number (IQ value[14]) indicating the signal-to-background ratio (S/B), with the largest boxes and smallest numbers reflecting the best data (IQ = 1, S/B > 7.0; IQ = 2, S/B > 3.5; IQ = 3, S/B > 2.3; IQ = 4, S/B > 1.8; IQ = 5, S/B > 1.4; IQ = 6, S/B > 1.2; IQ = 7, S/B > 1.0; IQ = 8, S/B > 0; IQ = 9, S/B < 0). Values from 1 to 4 are shown as numbers inside boxes, values from 5 to 8 are indicated by decreasing box size. The rings indicate zeros in the CTF. H and K indicate the reciprocal axes. **b**, Measured phases as a function of resolution. Each point represents the averaged phases for a given reflection from seven images. The cutoff for the data used here is indicated by a dashed line.

of reflections and measured phases as a function of resolution. Raw phases were rounded to 0° or 180° to impose strict two-fold symmetry on the projection, and phase residuals were calculated from the absolute values of the rounding errors. Although the averaged phase residuals are below random (45°) to 5.0 Å (Fig. 3), we used data only to 6.5 Å. In addition, only spots with a signal/background ratio $\geq$ 1.4 were used. In this merged dataset, the overall phase residual was 12.5°, with a 28.4° residual in the highest-resolution range used, 7–6.5 Å.

In projection normal to the membrane plane, EriC is a lens-shaped protein roughly 100 Å in length and 50 Å in width (Fig. 4a). A single unit cell contains two EriC channels; crystallographic two-fold axes lie within the protein and thereby confirm the expected homodimeric nature of the complex[2,11]. The protein–lipid boundary is unmistakable, with the flat, featureless lipid areas distinct from the steeply contoured higher density of the protein. EriC shows two pairs of remarkably low-density troughs, ~8 Å and ~5 Å in width, each pair separated by a density peak ~7 Å across. These trough-densities are substantially lower than the lipid density observed between the channel complexes (Fig. 4b).

Of the substances present on the sample grid—protein, lipid, water and glucose—the weakest scatterer is water[12]. This fact alone identifies the low-density wells as aqueous cavities of significant extension normal to the membrane plane. Although much of the water on the sample will have evaporated during the time that the grid was at high vacuum and not yet frozen, we presume that the water present in these cavities is either tightly bound to the protein or trapped by a thin layer of dried glucose. To obtain a more quantitative sense of these features, we calibrated the observed densities using the known scattering densities of lipid and protein, and by assuming that the lipid region represents acyl chains in a bilayer of 30 Å thickness. We then estimate the thickness of the low-density wells to be ~25 Å, consistent with aqueous pathways extending through a substantial fraction of the protein.

Because ~50% of EriC's mass is predicted to lie outside the transmembrane domains, the protein probably extends beyond the acyl-chain region of the lipid bilayer. Therefore, neither aqueous cavity is likely to be long enough to traverse the entire protein, but

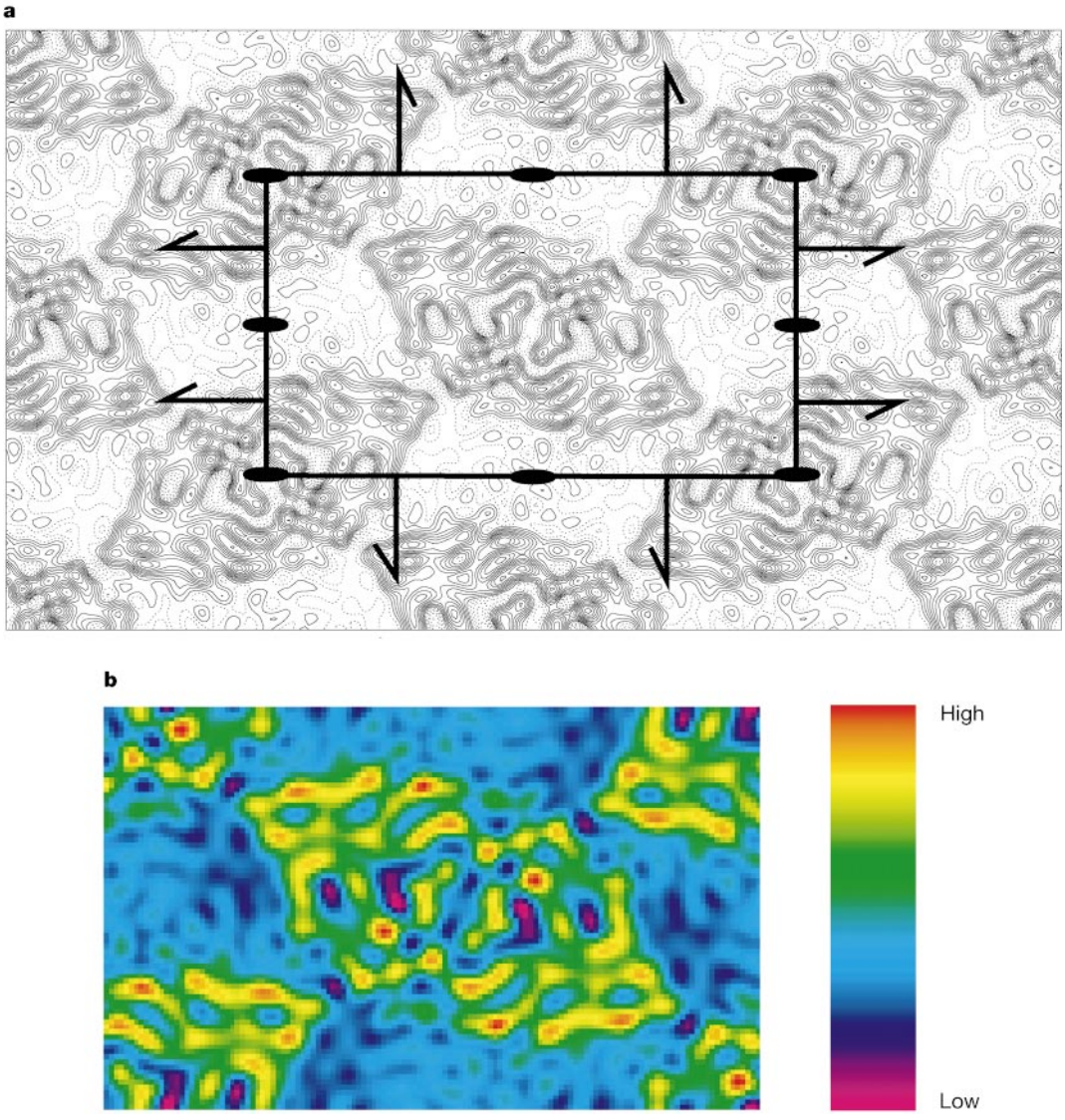

Figure 4 Projection density map of EriC at 6.5 Å resolution. **a**, Contour map of EriC calculated from merged data obtained from seven crystals. A unit cell is boxed with the *a* axis (140 Å) horizontal and the *b* axis (80 Å) vertical in two-sided plane group $P22_12_1$. The two-fold axes perpendicular to the membrane plane and the screw axes parallel to the membrane plane are indicated (with the central two-fold axis omitted for clarity). The zero contour level is roughly the average density of the lipid area; negative and positive contours are shown as dotted and solid lines, respectively. **b**, Colour-coded EriC density map. A single unit cell is plotted using the same data as in **a** with densities colour coded according to the scale on the right.

the two taken together could comfortably span its width. For this reason, we propose that each pair of density wells represents a single pore kinked roughly halfway along its length, such that the intracellular and extracellular openings are offset when viewed in projection normal to the membrane plane. This model, which implies two such pores in the dimeric channel, provides a natural structural rationale for the double-barrelled gating behaviour of single ClC channels from eukaryotes, and supports the previous inference that ClC channel pores cannot be axially symmetric[1,7]. In addition, with a separation of 25–40 Å, the two pores would, as expected, be far enough apart for them to be electrostatically independent at the physiological 10 Å Debye length[1].

The fact that EriC, a prokaryotic protein, provides a faithful structural explanation of the gating of eukaryotic ClC channels supports the proposal that double-barrelled architecture is a fundamental, evolutionarily conserved feature of the entire ClC family[11]. The absence of a strong low-density well on the dimer's two-fold axis is inconsistent with a symmetric one-pore construction for this channel. Of course, a definitive picture of the pore's transmembrane path must await three-dimensional information emerging from images of tilted crystals.

Transmembrane topology of ClC channels is uncertain; hydrophobicity analysis predicts 10–12 membrane-spanning segments[13], and the cytoplasmic location of amino and carboxy termini demands an even number of membrane crossings. At 6.5 Å resolution, untilted transmembrane α-helices should produce strong circular density peaks in projection, and four such peaks are easily discerned in each EriC monomer. Additional elongated density peaks may represent tilted helices or other secondary structure. We count 12 peaks in all, but this projection map is insufficiently detailed to distinguish 10 from 12, and three-dimensional information will be required to identify all the transmembrane helices. Previous work on mammalian ClC-1 (ref. 9) characterized an externally exposed, putative pore-lining residue just preceding the fourth transmembrane segment (D4) that can be disulphide-cross-linked to its dimeric twin when substituted by cysteine, a reaction that localizes this residue near the two-fold axis of the dimer. In the EriC structure only one prominent density peak lies close to the two-fold axis in each monomer; notably, this density also abuts the larger of the pore openings. We thus speculate that this strong density represents D4. If this region undergoes a conformational change with gating, residues that line the pore in the open state might face the symmetry axis when the channel is closed. Therefore, crosslinking across the two-fold axis would lead to functional inhibition, as observed in ClC-1, by trapping a closed conformation of the channel. This conjecture predicts that the crosslinking should be dependent on conformational state, with reaction occurring only in the closed form of the channel. □

Methods

Crystal formation

EriCΔa, a decahistidine-tagged variant also lacking the five carboxy-terminal amino acids, was expressed in *Escherichia coli* through vector pASK–IBA2 (kindly provided by A. Skerra) using a tetracycline promoter, and was purified as described[2] with minor modifications. Pure EriC, with the His-tag proteolytically removed, was mixed with synthetic palmitoyl-oleyl-phosphatidylcholine (POPC) at a lipid/protein mass ratio of 0.4 (molar ratio ~50) in 4 mM decylmaltoside (DM). The mixture was dialysed against several changes of a solution containing 25 mM NaCl, 20 mM $MgCl_2$, 20 mM Tris-HCl, 0.8 mM NaN_3, pH 7.0. Crystals were collected and stored at 4 °C. Samples were screened for crystallization by electron microscopy using 1% uranyl acetate as negative stain. Unstained specimens were prepared for high-resolution microscopy by deposition on carbon-coated copper grids, followed by embedding in 1% glucose with 0.25 mg ml^{-1} bacitracin as a wetting agent. Samples were immediately transferred to the electron microscope and cooled by liquid nitrogen *in situ* in a Gatan cryo-stage.

$^{36}Cl^-/^3H$[glutamate] double-label flux assay

The two-dimensional crystals were collected by centrifugation at 3,000*g* (5 min), washed with dialysis buffer, and then extracted with 10 mM DM (room temperature, 1 h). Equilibrium exchange of vesicle-entrapped $^{36}Cl^-$ was measured as described[2]. Briefly, EriC was reconstituted at varying concentrations into vesicles (500 μg lipid per sample) in the presence of the radioactive tracers $^{36}Cl^-$ and ^3H[glutamate]. $^{36}Cl^-$ release was initiated by diluting the vesicles ninefold into tracer-free solution, and the entrapped $^{36}Cl^-/^3H$[glutamate] counts were determined 2.5–3.5 h after dilution.

Electron microscopy

Electron micrographs were recorded in the Hitachi HF2000 FEG microscope at the MRC, Cambridge, England, at an accelerating voltage of 200 kV and nominal magnification of ×60,000. Magnification was later calibrated with tobacco mosaic virus. Unstained, glucose-embedded samples were imaged under low-dose conditions, ~5–15 electrons per $Å^2$, using Kodak SO163 film. Micrographs were screened by optical diffraction, and only those with evenly distributed spots extending to at least 10 Å resolution were used for final analysis.

Image processing

Well-ordered areas of 5,000 × 5,000 pixels were scanned at 7 μm per pixel using a Zeiss SCAI scanner, and computationally reduced to 14 μm per pixel. Data were corrected for lattice distortions, the contrast transfer function (CTF) and astigmatism using the MRC image processing programs[14,15]. Two passes of unbending were used, with a reference area of 200 × 200 pixels in the first pass and 150 × 150 pixels in the second. The image amplitudes were scaled as a function of resolution to compensate for resolution-dependent attenuation, using the program SCALIMAMP3D with bacteriorhodopsin as reference[16].

Received 25 August; accepted 30 October 2000.

1. Maduke, M., Miller, C. & Mindell, J. A. A decade of CLC chloride channels: structure, mechanism, and many unsettled questions. *Annu. Rev. Biophys. Biomol. Struct.* **29,** 411–438 (2000).
2. Maduke, M., Pheasant, D. J. & Miller, C. High-level expression, functional reconstitution, and quaternary structure of a prokaryotic ClC-type chloride channel. *J. Gen. Physiol.* **114,** 713–722 (1999).
3. Jentsch, T. J. & Gunther, W. Chloride channels: an emerging molecular picture. *BioEssays* **19,** 117–126 (1997).
4. Ludewig, U., Pusch, M. & Jentsch, T. J. Two physically distinct pores in the dimeric ClC-0 chloride channel. *Nature* **383,** 340–343 (1996).
5. Ludewig, U., Pusch, M. & Jentsch, T. J. Independent gating of single pores in CLC-0 chloride channels. *Biophys. J.* **73,** 789–797 (1997).
6. Miller, C. Open-state substructure of single chloride channels from Torpedo electroplax. *Phil. Trans. R. Soc. Lond. B* **299,** 401–411 (1982).
7. Middleton, R. E., Pheasant, D. J. & Miller, C. Homodimeric architecture of a ClC-type chloride ion channel. *Nature* **383,** 337–340 (1996).
8. Saviane, C., Conti, F. & Pusch, M. The muscle chloride channel ClC-1 has a double-barreled appearance that is differentially affected in dominant and recessive myotonia. *J. Gen. Physiol.* **113,** 457–468 (1999).
9. Fahlke, C., Rhodes, T. H., Desai, R. R. & George, A. L. Jr. Pore stoichiometry of a voltage-gated chloride channel. *Nature* **394,** 687–690 (1998).
10. Valpuesta, J. M., Carrascosa, J. L. & Henderson, R. Analysis of electron microscope images and electron diffraction patterns of thin crystals of phi 29 connectors in ice. *J. Mol. Biol.* **240,** 281–287 (1994).
11. Middleton, R. E., Pheasant, D. J. & Miller, C. Purification, reconstitution, and subunit composition of a voltage-gated chloride channel from Torpedo electroplax. *Biochemistry* **33,** 13189–13198 (1994).
12. Grigorieff, N., Beckmann, E. & Zemlin, F. Lipid location in deoxycholate-treated purple membrane at 2.6 Å. *J. Mol. Biol.* **254,** 404–415 (1995).
13. Jentsch, T. J., Steinmeyer, K. & Schwarz, G. Primary structure of Torpedo marmorata chloride channel isolated by expression cloning in *Xenopus* oocytes. *Nature* **348,** 510–514 (1990).
14. Henderson, R., Baldwin, J. M., Downing, K. H., Lepault, J. & Zemlin, F. Structure of purple membrane from halobacterium halobium: recording, measurement and evaluation of electron micrographs at 3.5 Å resolution. *Ultramicroscopy* **19,** 147–178 (1986).
15. Crowther, R. A., Henderson, R. & Smith, J. M. MRC image processing programs. *J. Struct. Biol.* **116,** 9–16 (1996).
16. Schertler, G. F., Villa, C. & Henderson, R. Projection structure of rhodopsin. *Nature* **362,** 770–772 (1993).

Acknowledgements

We are grateful to R. Henderson for making facilities at the MRC, including the Hitachi microscope, available to us for low-dose experiments, to J. Berriman for help and hand-holding, and to T. Walz for crucial advice on crystallization. We also acknowledge D. Pheasant and L. Melanson for technical assistance. Support was provided in part by a grant to J.A.M. from the NIH.

Correspondence and requests for materials should be addressed to J.A.M. (e-mail: jmindell@brandeis.edu).